Thermomagnetic liquid metal switches with fast bidirectional response

Haodong Chen[1], Yuyu Xie[1], Kaiming Qiao[1], Longlong Xie[1], Ziyuan Yu[1], Chenyu Xu[1], Jingyi Liu[1], Mingze Liu[1], Yongyu Lu[2], Jing Liu [2], Fengxia Hu [3], Baogen Shen[3], Ke Chu [4], Jia Yan Law [5], Victorino Franco [5] & Hu Zhang [1] ✉

Traditional thermal switches usually suffer from long-time and unidirectional response. Herein, we combined liquid metals with magnetic $Ni_2Mn_{1.4}In_{0.6}$ particles and developed a thermomagnetic liquid metal. These materials not only show excellent fluidity and electrical conductivity, but also exhibit fast response at a tuneable temperature that traditional magnetic liquid metals do not have. The ultimate application is designed as micro-channel thermal switch. Particularly, our thermal switch features bidirectional response through the droplet displacement, thus simultaneously cutting off the working circuit while turning on the fire extinguishing. Its response time of 1.2 s is 3.3 − 5.6 times faster than typical commercial thermal switches under the same hot source temperature of 75 °C, and it can be further reduced to 660 ms under the optimal environment. Moreover, this fast-response thermal switch offers the fastest recovery time, low cost, and long-cycle stability, showing a huge potential as a generation of thermal switches for diverse applications.

Localized overheating of electric circuits can be seen almost everywhere in daily life and industrial production (Fig. 1a). However, localized temperature buildups can often go unnoticed until they escalate and transform into high-temperature environments or large-scale flames[1], leading to devastating consequences. In such cases, the rapid spread of flames hinders timely control and extinguishment, resulting in significant casualties and irreparable property losses[2]. Analysis of fire statistics over the past decade found that electrical fires accounted for the highest proportion of all fire types (see Fig. 1b), and have remained at about 30% for long time, posing a serious threat to human life and property safety as well as ecological environment[3]. Rapid detection and response to electrical fire hazards, especially in the critical few seconds after ignition, are essential for minimizing damage and saving lives. Even a few seconds' delay in detection can substantially increase fire size, smoke inhalation, and property damage[4]. However, most commercial thermal switches and smoke detectors respond within several seconds to over 100 seconds, this highlights the urgent need for faster thermal switches to enable early detection and rapid suppression, thus preventing loss of life and property.

Thermal switches, serving as a pivotal thermal response control element, offer a crucial and widespread solution in many scenarios, such as equipment protection and fire suppression[4]. By promptly triggering (switch ON/OFF) in response to elevated temperatures, thermal switches help mitigate the risk of overheating hazards and issue timely warnings of overheating. Generally, thermal switches can be classified into three categories based on their working principles: gas/smoke sensors[5,6], resistance-shift switches[7], and shape-change switches[8,9]. The gas/smoke sensors are the most common thermal switches used in many practical applications of fire warning[5], which can not only trigger the sprinkler system but also alert the fire department. However, they are prone to false alarms caused by non-fire-related smoke (e.g., cooking or dust), leading to unnecessary disruptions and desensitization to alarms. Moreover, their response time usually takes longer than 100 s, limited by the relatively low

[1]School of Materials Science and Engineering, University of Science and Technology Beijing, Beijing 100083, P R China. [2]Key Laboratory of Cryogenic Science and Technology, Technical Institute of Physics and Chemistry, Chinese Academy of Sciences, Beijing 100190, P R China. [3]Beijing National Laboratory for Condensed Matter Physics, Institute of Physics, Chinese Academy of Sciences, Beijing 100190, P R China. [4]School of Materials Science and Engineering, Lanzhou Jiaotong University, Lanzhou 730070, P R China. [5]Multidisciplinary Unit for Energy Science, Dpto. Física de la Materia Condensada, ICMS-CSIC, Universidad de Sevilla, P.O. Box 1065, 41080 Sevilla, Spain. ✉e-mail: zhanghu@ustb.edu.cn
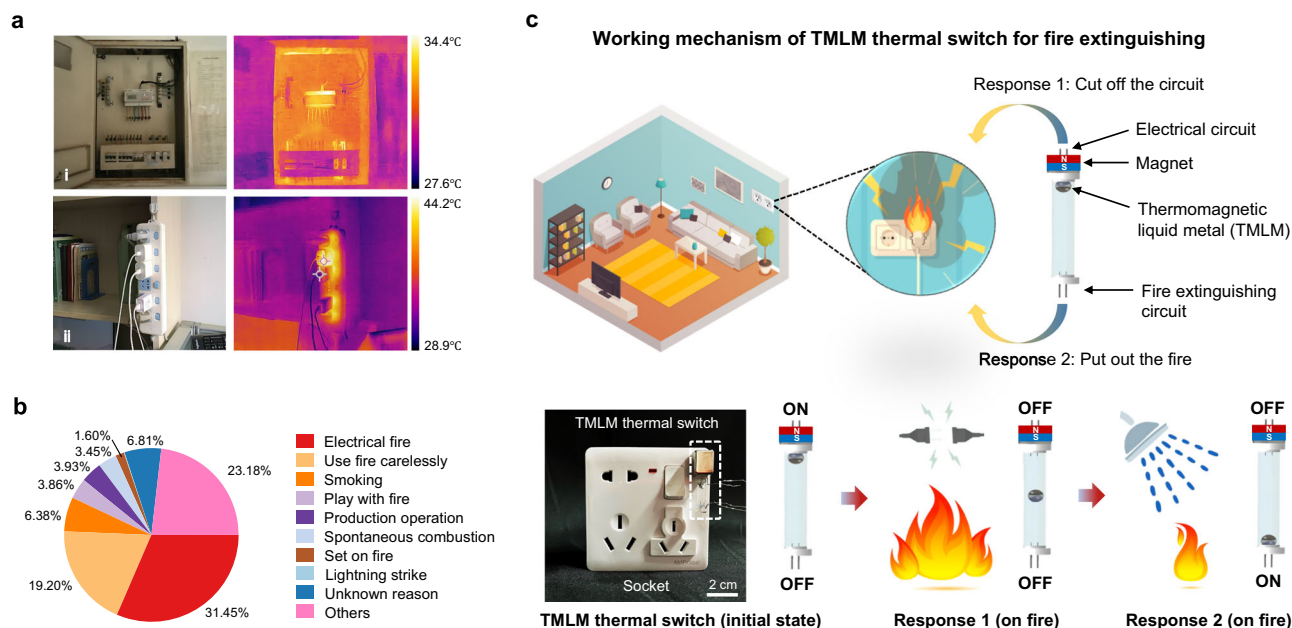
Fig. 1 | The huge proportion of electrical fires, as well as the concept and advantages of the TMLM thermal switch for fire extinguishing. a Infrared photos of localized overheating of electric circuits. **b** The average proportion of various fire types in the past decade. **c** Schematic illustration and working principle of TMLM thermal switch with fast bidirectional response for fire extinguishing. (Elements in Fig. 1c, created with freepik.com, released under a license. Source data are provided as a Source Data file).

sensitivity[6], resulting in a failure to provide a fast response to incipient fires. In contrast, the resistance-shift switches undergo a transition from insulator to conductor, significantly increasing electrical conductivity, thus boasting a relatively fast response time of ~8 s with the "sandwich-like" structure[7], or even 0.25 s for an amino-functionalized carbon nanotube (CNT) aerogel[10]. Unfortunately, they usually suffer from unidirectional response, non-linear resistance changes, and poor long-term stability, which limits their practical application in complex circuits. On the contrary, shape-change switches can effectively disconnect one circuit while simultaneously connecting another, thanks to their shape-change abilities in response to temperature variations[8]. However, the low thermal conductivity and recovery stress of their working materials cause slow response times, which can extend to as long as 5 min[11]. In addition, due to the mechanical wear and fatigue issues, they also suffer from unstable contact resistance and limited cycle life[12]. Therefore, it is crucial to develop a thermal switch that can effectively address the limitations of the current traditional thermal switches.

Recently, liquid metals (LMs) have been widely reported to have many properties, including high electrical and thermal conductivity[13,14], high deformability[15,16], and low toxicity[17,18]. In addition, researchers have added Fe[19–21], iron oxides[22], and NdFeB[15,23] particles into LMs to obtain magnetic liquid metals (MLMs), which can be positioned by the attraction of a magnet. The MLMs can be driven by moving the magnet to function as magnetic switches[21,24]. However, these magnetic switches cannot be used as thermal switches due to the lack of thermosensitive property. Ni$_2$MnZ (Z = Al, Ga and In) Heusler alloys have attracted much attention due to their interesting thermal-induced magnetic and martensitic structural transitions[25–27]. Therefore, it can be expected to improve the thermosensitive property of MLMs by utilizing the thermomagnetic phase transition of Ni$_2$MnZ Heusler alloys, thus preparing a type of thermomagnetic liquid metal switches.

In this work, we chose Ni$_2$Mn$_{1.4}$In$_{0.6}$ (Ni-Mn-In) Heusler alloy with a ferromagnetic transition as thermosensitive magnetic material, and introduced its particles into LMs with oxidized mixing method to prepare a thermomagnetic liquid metal (TMLM). This TMLMs have good fluidity, appropriate viscosity, and high electrical conductivity. In addition, this TMLMs not only can be driven by a magnetic field like traditional MLMs, but also exhibits fast temperature sensitive characteristics that traditional MLMs do not possess. Although a few works have been reported on mixing magnetocaloric materials with Galinstan[28–30], they primarily focused on the magnetocaloric effect. Unlike those works, based on the special advantages of TMLMs, we designed a micro-channel thermal switch by using this TMLMs. As the TMLM thermal switch offers fast bidirectional response, it can be hypothesized as an ideal solution for promptly suppressing circuit fires. Unlike traditional circuit safety switches, which disconnect the circuit only after it overheats (but do not activate the fire extinguishing equipment), the TMLM thermal switch can mitigate the fire promptly by quickly activating the fire extinguishing equipment in a simple way. This approach would help prevent property damage and loss of life by addressing circuit fires more effectively. The concept of TMLM potentially addressing circuit fires is schematically illustrated in Fig. 1c, where the TMLM thermal switch is positioned on a socket. The upper end of the thermal switch is connected to the electrical circuit within the socket, while the lower end is connected to a fire extinguishing circuit. In the event of the electrical circuit catching fire, the TMLM thermal switch on the socket will deactivate the electrical circuit, concurrently, activating the fire extinguishing circuit through the release (falling) of the conductive TMLM droplet. This rapid response will promptly and effectively extinguish the fire. The temperature response time of this TMLM thermal switch is 3.3 – 5.6 times faster than those of other typical commercial thermal switches. Moreover, it can recover quickly for long-term recycling. These advantages suggest that this TMLM has great potential for application in thermal switches, especially in the field of microcircuit thermal management.

Results
Synthesis, morphology, and structure of TMLMs
The TMLMs with Ni-Mn-In particles are synthesized according to the schematic presentation in Fig. 2a. Firstly, Ni-Mn-In ingot was prepared
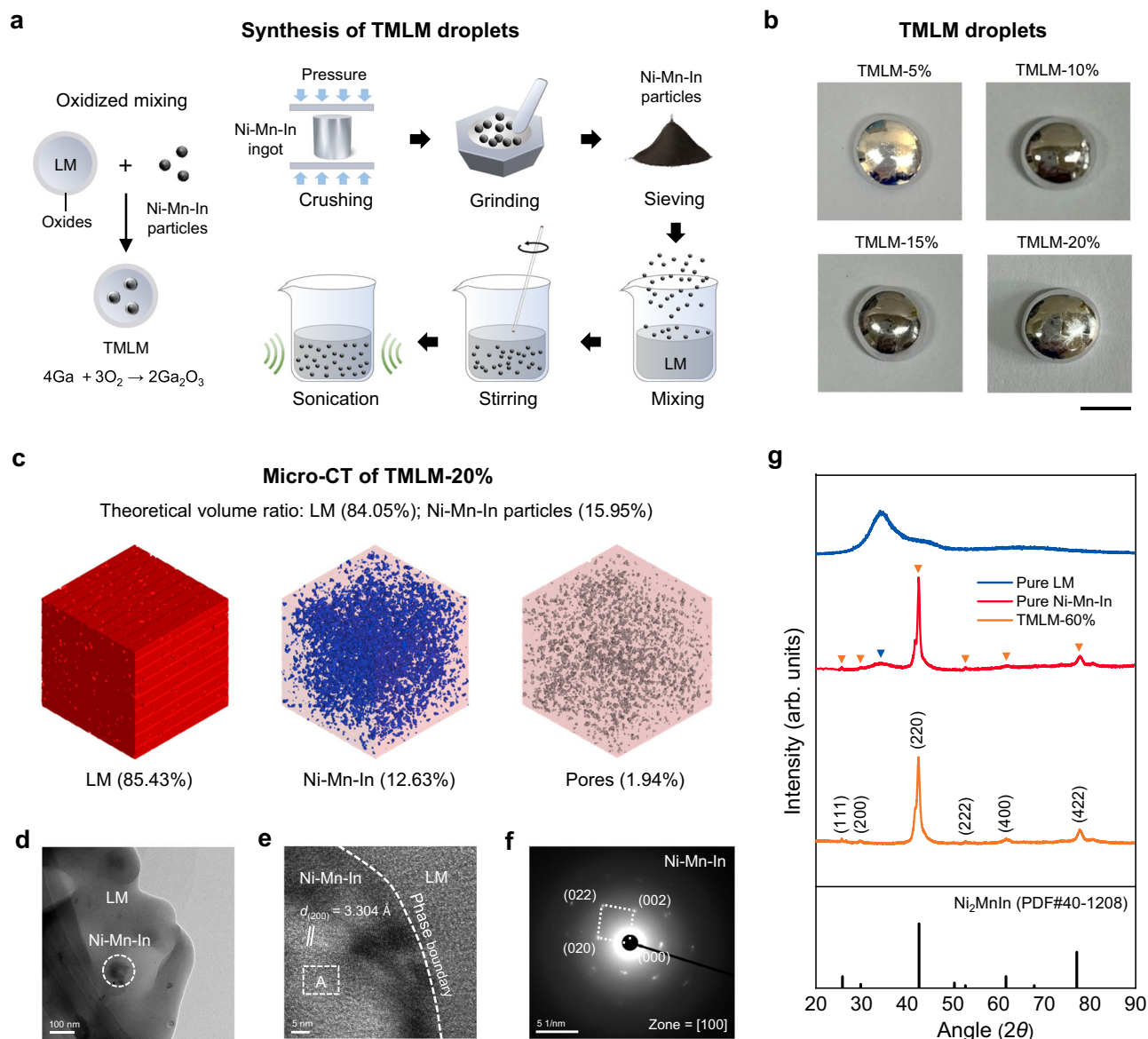
Fig. 2 | Synthesis, morphology, and structure of the TMLM droplets. a Synthesis of the TMLM droplets. **b** Photographs of TMLM droplets with different packing fractions of 5, 10, 15, and 20 wt.% (Denoted as TMLM-x%, x% refers to the mass fraction of Ni-Mn-In particles in TMLM droplets). **c** Micro-computed tomography (micro-CT) of TMLM-20%, where the 3D images show the distribution of low-density liquid metal phase (red), high-density Ni-Mn-In particles (blue), and pores (gray), respectively. **d** Bright-field image at room temperature for an area with coexisting LM and Ni-Mn-In particle in TMLM-20%. **e** High-resolution transmission electron microscopy (HRTEM) image for coexisting LM and Ni-Mn-In particle in TMLM-20%. **f** Selected area diffraction pattern (SADP) for the cubic $L2_1$ austenite along [100] zone axis, corresponding to the dashed frame A in panel (**e**). **g** XRD characterization of pure LM, pure Ni-Mn-In, and TMLM-60% (left for 21 days). Blue and yellow symbols represent the characteristic peaks of LM and Ni-Mn-In, respectively. (Source data are provided as a Source Data file).

by induction-melting from elemental raw materials, followed by annealing. It was then crushed into particles and sieved, obtaining an average diameter of ~37.88 μm and with a uniform composition (Supplementary Figs. 1 and 2). An appropriate amount of Ni-Mn-In particles (5, 10, 15, and 20 wt.%) were introduced into Galinstan LM and vigorously stirred for about 15 – 30 min to achieve complete homogeneity. During the mixing process, the oxide layer on the LM surface is continuously broken to create new oxides, which will coat Ni-Mn-In particles. Because this new oxide coating is easily miscible with LM, the Ni-Mn-In particles were successfully incorporated into the LM. Finally, sonication treatment was used to make the Ni-Mn-In particles evenly distributed in the LM. Figure 2b shows the photographs of the four TMLMs containing different load of Ni-Mn-In magnetic particles, where all maintain a metallic luster and bead shape at room

temperature (RT) without exhibiting any curing behavior even for the higher packing fractions. This indicates that they all have good fluidity. Besides, their SEM images show that the Ni-Mn-In particles are uniformly distributed without obvious agglomeration in the two-dimensional plane (Supplementary Fig. 3).

An in-situ 3D micro-CT analysis of the TMLM-20% sample reveals the distribution of its different components in three-dimensional space (Fig. 2c): the Ni-Mn-In particles (marked in blue) are evenly dispersed in the LM (red region) without noticeable agglomeration or sedimentation, indicating that the TMLM exhibits both uniform and stable thermomagnetic particle distribution. Furthermore, their refined results show that the LM, Ni-Mn-In particles and pores have volume fractions of 83.01%, 12.83%, and 4.16%, respectively. These are in good agreement with the theoretical volume fractions. The robust

interfacial bonding between the LM and Ni-Mn-In is observed in the high-resolution transmission electron microscopy (HRTEM) investigations where its micrograph presents perfectly coated Ni-Mn-In particles by the LM in the nanoscale (Fig. 2d and Supplementary Fig. 4). It is also revealed that the Ni-Mn-In phase exhibits evenly arranged atomic layers with an interplanar spacing of 3.304 Å, which corresponds to the austenitic phase (Fig. 2e). Its selected area diffraction pattern (SADP) image further confirms the austenite characteristic of the cubic $L2_1$ Heusler structure with a zone axis of [100] (Fig. 2f). The LM region, on the other hand, has an amorphous structure where an obvious phase boundary is observed between the LM and Ni-Mn-In regions. No impurity phase is observed near the phase boundary, suggesting the absence of alloying reactions between the LM and Ni-Mn-In particles, a phenomenon typically associated with LM and doped particles. Such reactions have the potential to compromise the functional properties of the doped particles. The collective observations, in conjunction with the low porosity volume, not only indicate a robust interfacial bonding between the LM and Ni-Mn-In particles but also establish that the entire TMLM will exhibit a high degree of responsiveness when subjected to a magnet, thanks to the good dispersion of the thermomagnetic particles.

In order to investigate the possibility of alloying reactions between liquid metals and Ni-Mn-In particles, a significantly higher load, 60 wt.% Ni-Mn-In particles was used, as that would facilitate the detection of this effect. After leaving the TMLM-60% sample for 21 days, X-ray diffraction experiments were performed to compare their resulting phase with constituents, pure LM and Ni-Mn-In particles, as shown in Fig. 2g. Pure LM shows a broad diffraction halo around 26.2° ~ 47.6°, corresponding to the typical characteristic of an amorphous phase, which agrees with TEM observations. The Ni-Mn-In diffraction pattern shows a single austenitic phase with $L2_1$ structure (space group $Fm3m$) at RT, with lattice parameter $a = 6.024$ Å. As for the TMLM-60%, it exhibits both characteristic behavior of Ni-Mn-In (diffraction peaks) and amorphous LM (broad halo) with no other characteristic peaks present. This re-affirms that no alloying behavior occurs between LM and Ni-Mn-In particles even after a long time, proving the long-term stability of TMLMs.

Characterization and magnetic actuation performance of TMLMs

Figure 3a shows the elastic modulus G' and viscous modulus G'' as a function of shear stress for TMLMs. At low shear stress, up to ~70 Pa, all the TMLMs maintain elastic-dominant behavior in the linear viscoelastic region where $G' > G''$. Shear stress causes the decrease of G' while G'' gradually increases, and they eventually intersect at the critical shear stress τ_0, implying that the fluidity of TMLMs begins to surpass its elasticity. It is noted that τ_0 only increases slightly with the increase of packing fraction, indicating that the TMLMs maintain as good fluidity as the pure LM. Furthermore, the contact angles of TMLMs show a slight increase with higher packing fractions, as depicted in Fig. 3b, consistent with the rising trend of apparent viscosity with doping fractions (Supplementary Fig. 5). This arises as the increased apparent viscosity induces a decrease in surface tension, thus leading to an increase in contact angle. Moreover, since the TMLM still maintains the bead shape of a LM, it indicates that the TMLM shows similar fluidity to pure LM, despite having a higher apparent viscosity. These collective findings signify that the current TMLMs demonstrate excellent fluidity and viscosity comparable to pure LM.

Figure 3c compares the electrical conductivities of pure LM and TMLMs with different thermomagnetic filler concentrations. Although Ni-Mn-In has a relatively low electrical conductivity (0.71×10^6 S m^{-1})[31] compared to pure LM (2.12×10^6 S m^{-1} at RT), incorporation of the Ni-Mn-In particles into the LM results in only a minor decrease in electrical conductivity, with the overall electrical conductivity remaining relatively high at ~2.0×10^6 S m^{-1}. Even when the filler content reaches

60 wt.%, it still remains as high as 1.91×10^6 S m^{-1}. The high fluidity of LM allows it to maintain a dense and continuous structure even after doping with a high particle fraction. As a result, the low-resistance conductive path will hardly be changed by the doped high-resistance particles, making the electrical conductivity of TMLMs remain high, which is advantageous for their effective performance in circuit control applications.

Figure 3d shows the temperature (T) dependence of zero-field-cooling (ZFC) and field-cooling (FC) magnetization (M) under 0.4 T for pure $Ni_2Mn_{1.4}In_{0.6}$ alloy. The $Ni_2Mn_{1.4}In_{0.6}$ alloy experiences a typical first-order martensitic transition (FOMT) from ferromagnetic (FM) austenite to weak-magnetic martensite around 0 ~ −20°C with distinct thermal hysteresis. In addition, another second-order magnetic transition (SOMT) of austenite from FM to paramagnetic (PM) states appears at Curie temperature (T_C) of 43°C above the martensitic transition. The inset shows that the thermal hysteresis of FOMT is as large as ~10°C. This large thermal hysteresis causes different magnetizations as well as transition temperatures during heating and cooling, which would lead to inconsistent response temperature and response time of the thermal switch. These drawbacks indicate that it is not suitable to utilize the FOMT to design TMLM thermal switch. On the contrary, the SOMT in Ni-Mn-In alloy exhibits a perfectly reversible FM − PM transition without thermal hysteresis. Moreover, it shows a large magnetization change and high magnetocaloric effect (Supplementary Fig. 6), which is conducive to the fast response of the TMLM thermal switch. In addition, the SOMT does not generate large dislocation density and internal stress that easily leads to fracture failure like the FOMT. So it is favorable to obtaining better mechanical stability and longer service life than FOMT[32]. The above results indicate that the SOMT in Ni-Mn-In alloy is suitable for the design of thermal switch.

Furthermore, Fig. 3e shows the $M − T$ curves for TMLMs with different Ni-Mn-In contents. Similar to the pure Ni-Mn-In alloy, all the TMLMs also undergo a FOMT followed by a SOMT with increasing temperature. This suggests that the thermomagnetic properties of TMLMs are attributed to the incorporation of Ni-Mn-In particles into the liquid metal, which results in the rapid thermomagnetic response of the TMLM thermal switch. Meanwhile, the T_C values of all TMLMs remain stable around 43°C, indicating the thermomagnetic transition of Ni-Mn-In particles is not affected upon mixing with LM for creating the TMLMs. Moreover, the magnetization of TMLMs increases with higher Ni-Mn-In particle packing fractions, revealing the enhancement of ferromagnetism. The above results prove that the magnetic properties of TMLMs are predominantly determined by the Ni-Mn-In component, and so the magnetization will keep rising with the Ni-Mn-In content further increasing even higher than 20 wt.%. The magnetization of TMLM-20% changes sharply from the maximum value of 5.4 Am^2 kg^{-1} to nearly zero during the SOMT, which is highly suitable for the design of a magnetic thermal switch.

Figure 3f compares the DSC curves during cooling and heating of pure LM, pure Ni-Mn-In, and TMLM-20%, respectively. For pure LM, the small peak at −9.0°C (T_1) indicates the onset of crystal nucleation during cooling, while the sharp peak observed at −44.5°C (T_2) corresponds to the completion of LM crystallization, consistent with literature[30,33]. During heating, LM starts to melt at 18.9°C (T_3), indicating that LM is a completely molten liquid at RT and thus has high fluidity. The difference between the melting and freezing temperatures is due to the supercooling nature of pure LM. On the other hand, pure Ni-Mn-In shows a structural transition from martensite to austenite, and vice versa, at temperatures T_{M-A} and T_{A-M}, with a large hysteresis, as well as a reversible SOMT at $T_C = 40.3°C$. These are consistent with the thermomagnetic results. For TMLM-20%, its DSC results reveal the occurrence of structural transformation and T_C (same as that of Ni-Mn-In), consistent with those observed from $M(T)$ curves. While TMLM-20% has T_2 comparable to that of pure LM, T_3
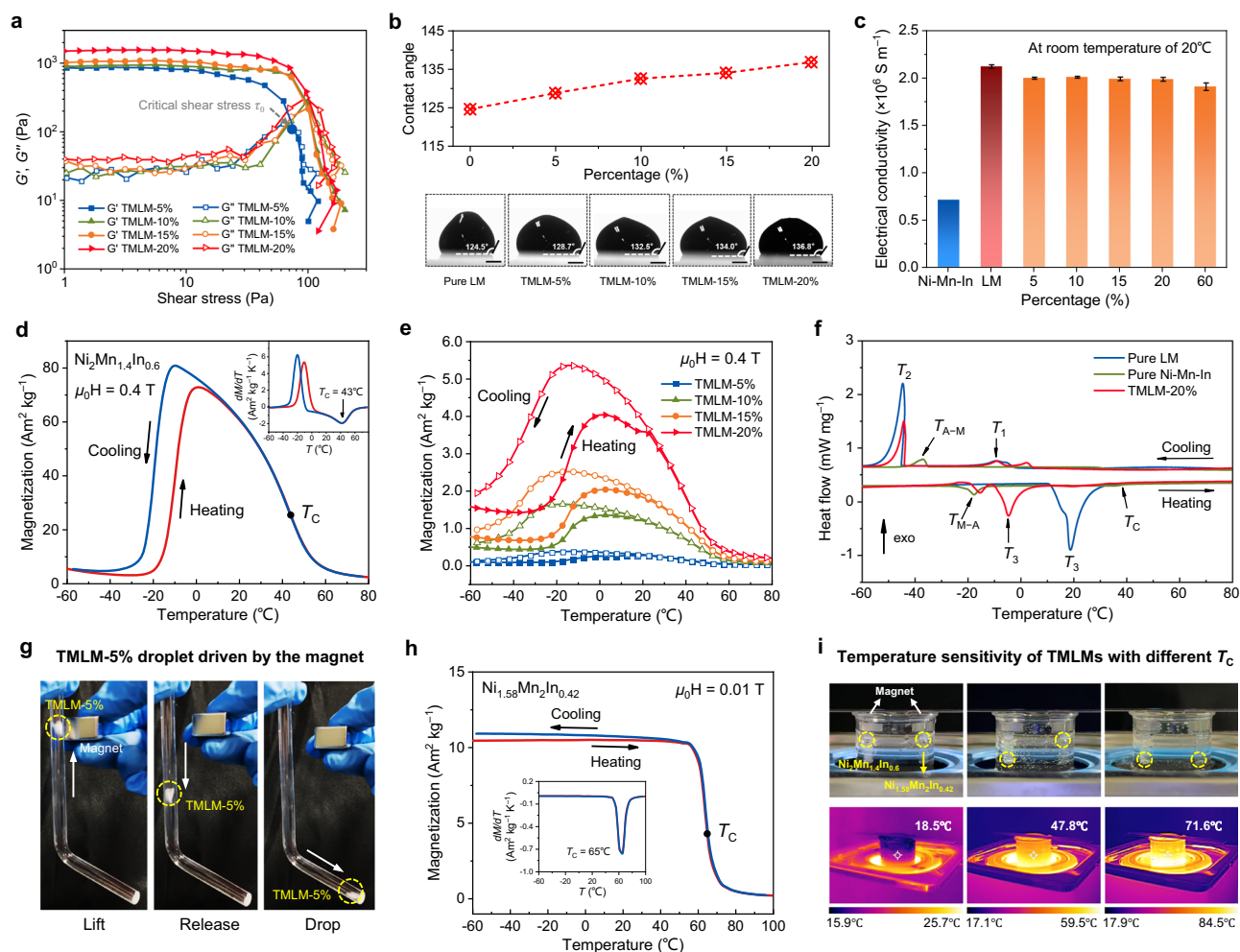
Fig. 3 | Physical properties and magnetic actuation performance of TMLMs.
a Oscillatory rheological test of TMLMs with different packing fractions. G′ and G″ are the elastic modulus and viscous modulus, respectively. **b** Contact angle as a function of packing fraction for TMLM droplets. The second row shows the droplet shape of pure LM and TMLMs with different packing fractions. Scale bars, 1 mm. **c** Electrical conductivity of Ni-Mn-In alloy, pure LM, and TMLMs with different packing fractions. Error bars indicate the standard deviation of three measurements. **d** Magnetization (M) as a function of temperature (T) at a magnetic field of 0.4 T for $Ni_2Mn_{1.4}In_{0.6}$ alloy. The inset shows the corresponding $dM-dT$ curves.

Solid symbols: heating, empty symbols: cooling. **e** The $M-T$ curves at 0.4 T for TMLMs with different packing fractions. **f** DSC curves of pure LM, pure Ni-Mn-In, and TMLM-20% measured during heating and cooling (negative values for heating and positive values for cooling). **g** Vertical control of the TMLM-5% droplet by using the magnet. **h** The $M-T$ curves for another Ni-Mn-In Heusler alloy with composition of $Ni_{1.58}Mn_2In_{0.42}$. **i** Experimental demonstration and infrared thermal images of the temperature sensitivity for TMLMs with different T_C. (Source data are provided as a Source Data file).

shifts distinctly from 18.9 (pure LM) to −4.5°C, which suggests that the introduction of thermomagnetic particles reduces the supercooling of LM[30,34]. Consequently, the melting temperature can be lowered, which will benefit a high fluidity of the TMLM around RT. Furthermore, through the inclusion of Ni-Mn-In particles, the least loaded TMLM droplet (TMLM-5%) is easily channeled up a bent tube by a magnet (and smoothly falls to the bottom upon removal of the magnet due to the gravity) as presented in Fig. 3g, further demonstrated for its magnetic actuation in crooked channels and petri dish (Supplementary Fig. 7 and Movie 1). In addition to the characteristic magnetic-driven behavior, our TMLM demonstrates good thermomagnetic responses: the TMLM-5% droplet placed at a cold side, i.e., temperatures below its T_C, can be FM-held by a magnet and ultimately drops off as the temperature rises beyond the T_C (the droplet transits to a PM state) as shown in Supplementary Fig. 8. This demonstrates that the TMLMs, tackling with their characteristic fast thermal-induced magnetic transition, can aid the response time of a thermal switch unlike typically reported magnetic liquid metals, which are not sensitive to temperature[15,19–21,24]. These attributes present distinct advantages not

found in conventional LM and magnetic LM circuits, making them highly desirable for designing the next-generation magnetic liquid metal thermal switch.

Since the T_C can be tuned by changing the composition of thermomagnetic transition materials, the operating temperature of the TMLMs can also be tuned accordingly. Figure 3h shows the $M-T$ curves for another Ni-Mn-In Heusler alloy with different composition of $Ni_{1.58}Mn_2In_{0.42}$. The inset reveals that the T_C of $Ni_{1.58}Mn_2In_{0.42}$ is 65°C, higher than that of $Ni_2Mn_{1.4}In_{0.6}$ (43°C). Then, we placed two types of TMLMs doped with $Ni_2Mn_{1.4}In_{0.6}$ and $Ni_{1.58}Mn_2In_{0.42}$ particles into a water bath, as shown in Fig. 3i. Initially, both TMLMs exhibited ferromagnetic behavior in the cold water at 18.5°C, allowing them to be attracted to the magnet. As the water temperature increased, the TMLM filled with $Ni_2Mn_{1.4}In_{0.6}$ detached from the magnet at 47.8°C, while the TMLM filled with $Ni_{1.58}Mn_2In_{0.42}$ detached at 71.6°C. This ability to adjust the T_C allows for the customization of TMLMs to meet specific temperature requirements, enhancing their versatility and performance in various thermal management applications.
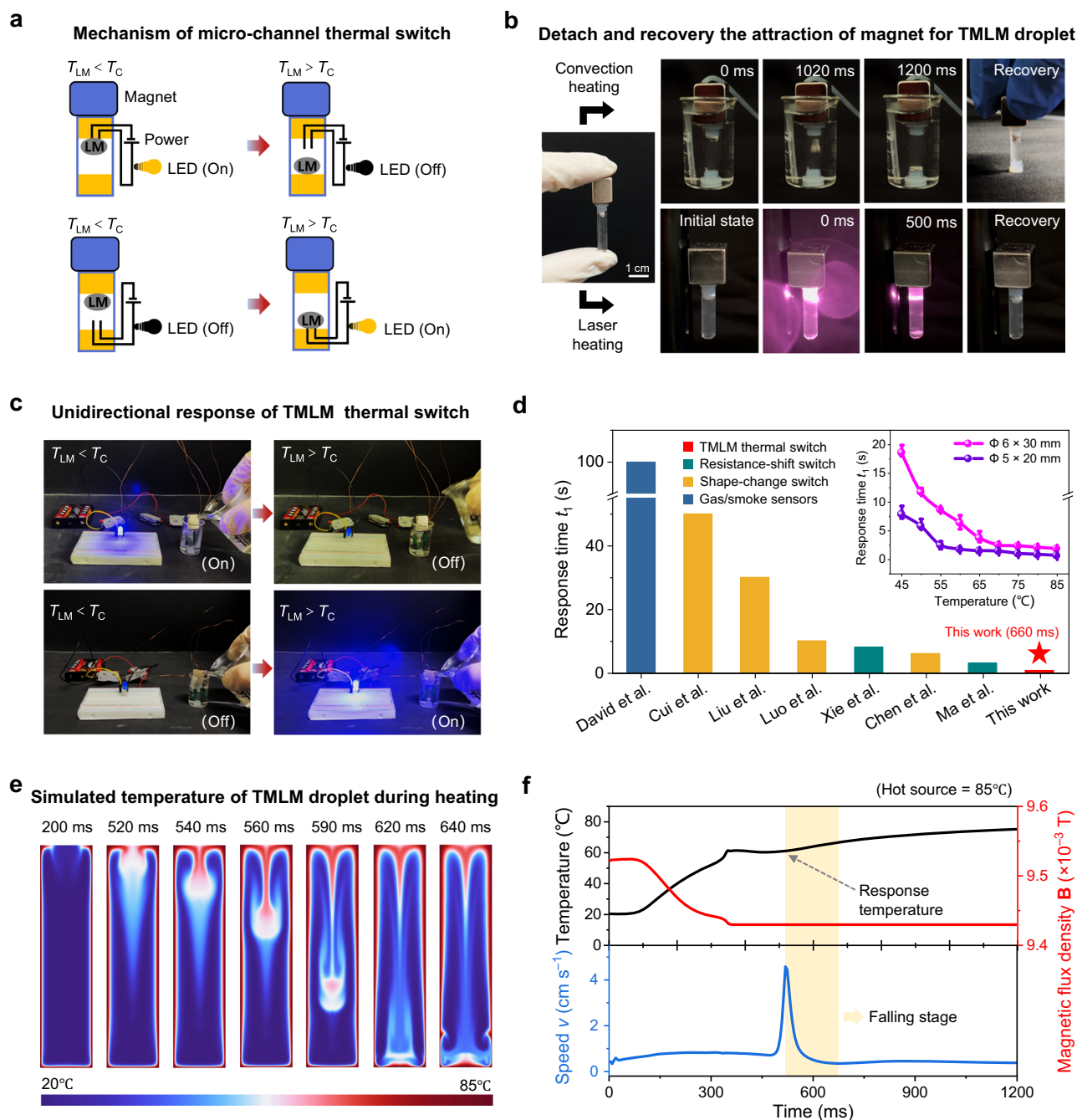
Fig. 4 | The unidirectional response of micro-channel TMLM thermal switches. **a** Schematic illustration of the working principle of micro-channel TMLM thermal switch. **b** Experimental demonstration of TMLM-20% droplet detach and recovery the attraction of magnet during heating and cooling. Two different heating methods are used: contact convection heating and non-contact laser heating. **c** Experimental demonstration of two unidirectional response modes of TMLM thermal switch. **d** Comparison of response time t_1 of TMLM thermal switch with those of reported different types of thermal switches. The inset shows t_1 of TMLM-20% droplet in two sizes of glass tubes as a function of hot source temperature. Error bars indicate maximum and minimum values. **e** Simulated temperature of a TMLM-20% droplet falling during heating. **f** The simulation results of the average temperature, magnetic flux density, and drop speed of TMLM-20% droplet as functions of time during heating, hot source = 85 °C. (Source data are provided as a Source Data file).

Micro-channel TMLM thermal switches

Based on the thermomagnetic-sensitive property of TMLMs, an advanced TMLM thermal switch was designed for a practical configuration: a micro-channel thermal switch using the TMLM droplet. As shown in Fig. 4a, a small TMLM droplet is housed within a thin glass tube. Initially, when the temperature of TMLM (T_{LM}) is lower than its T_C, the droplet is drawn towards the upper end of the tube by a small magnet, thus completing the LED circuit. Upon surpassing the T_C, the

droplet turns from FM to PM (due to the characteristic thermal-induced magnetic transition of TMLM), causing it to detach from the magnet and descend to the bottom, subsequently breaking the LED circuit. Similarly, the LED circuit can also be configured as a thermal-triggered conduction switch by positioning it at the lower end. In this case, the LED would illuminate upon the droplet detaching from the magnet as a result of overheating. Leveraging this design, we developed a miniature TMLM thermal switch using a TMLM-20% droplet. In

the experimental setup, both contact fluid convection heating and non-contact laser heating methods were used to facilitate the release of the TMLM droplet, as shown in Fig. 4b. A small droplet (volume of ~30 μL) consisting of TMLM-20%, is encapsulated in a glass tube that is filled with a commercial thermal fluid to enhance heat transfer. Moreover, this thermal fluid can also prevent direct contact between liquid metal and oxygen, and then reduces the formation of the oxide layer, leading to a good fluidity and thermomagnetic response of TMLMs (Supplementary Fig. 9). The droplet is held by the magnet, whose maximum field at RT is 0.4 T. It should be pointed out that the droplet can be lifted by a magnetic field $\mu_0 H$ lower than 200 mT, which is favorable for practical applications. Meanwhile, the distance between the magnet and TMLM droplet has been adjusted to 3.5 mm based on the relationship between the magnetic field and the distance between the magnet and the droplet (Supplementary Fig. 10). To assess the actuation of this tube thermal switch, we submerge it in a beaker containing hot water (at a temperature of 75°C) to replicate the heating process. Upon exposure to the external heat, the TMLM-20% droplet gradually detaches from the magnet's attraction and then assumes an ellipsoidal shape at 450 ms as a result of reduced surface tension[35]. Subsequently, at 1020 ms, it initiates detachment from the top, ultimately settling at the bottom at 1200 ms. Next, the micro-channel thermal switch is extracted from the beaker for air cooling. The TMLM droplet gets re-attracted to the top end, demonstrating its recovery to the FM state, which strongly indicates the potential for repeated utilization over multiple operational cycles. The entire process of actuating the micro-channel thermal switch has been recorded and is available for viewing in Supplementary Movie 2. The micro-channel TMLM thermal switch is susceptible not only to contact convection heat transfer, but also to non-contact heat transfer methods, such as radiation and laser heat transfers (Supplementary Movie 3). The laser-heating experiment demonstrates that the TMLM droplet takes only 500 ms to fall to the bottom when subjected to the laser, and subsequently returns to its FM state through air cooling, rapidly moving to the top end. These results prove the suitability of the TMLM thermal switch for diverse heating scenarios. Additionally, the tube thermal switch was further integrated into a LED circuit following the schematic diagram in Fig. 4a. The operation of the tube thermal switch activating and deactivating the LED circuit is captured and shown in Fig. 4c and Supplementary Movie 4. The observation reveals that the TMLM droplet detaches when subjected to heating, thereby causing the LED circuit to switch ON or OFF.

The response time (t_1), defined as the duration from the moment the switch contacts the heat source to the point at which the TMLM droplet detaches from the magnet, has been optimized by adjusting the size of the glass tube and the temperature of the heat source (T_H). The inset of Fig. 4d shows the t_1 of TMLM-20% droplet within two glass tubes varies as a function of T_H. For the same T_H, the t_1 in the smaller glass tube ($\Phi\ 5 \times 20$ mm) is significantly shorter than that in the larger tube ($\Phi\ 6 \times 30$ mm). This is because the smaller glass tube facilitates better heat conduction, making it advantageous for the design of a micro-size TMLM thermal switch. With increasing T_H, the t_1 in both glass tubes significantly reduces. This is because the tube temperature rises more rapidly under a higher T_H, and it takes a shorter time for the TMLM-20% droplet to reach T_C (Supplementary Fig. 11), leading to the shortening of t_1. In addition, the fast response time t_1 for the $\Phi\ 5 \times 20$ mm tube under $T_H = 85$°C can reach 660 ms under the optimal environment (Supplementary Fig. 12). It is noteworthy that the variance in response time among the tubes of different sizes diminishes significantly with increasing T_H, implying that T_H exerts a more pronounced influence on the response time. Furthermore, to ensure a fair comparison with different types of thermal switches, we selected three shape-change switches[36–38] that exposed to similar T_H ranging from 85 °C to 100 °C. Notably, an alcohol lamp (with an outer flame temperature of ~500°C) was used to trigger another shape-change switch[39]

and two resistance-shift switches[7,40]. Detailed heating methods and temperatures are shown in Supplementary Table 1. Figure 4d presents a comparison of the t_1 of our TMLM thermal switch with that of other types of thermal switches. Notably, the t_1 of our TMLM thermal switch substantially outperforms the other reported thermal switches. Specifically, even the T_H (~500°C) of the alcohol lamp is much higher than the 85 °C hot water bath used in our experiments, our TMLM thermal switch still exhibited a faster response time, which is between 1 and 2 orders of magnitude faster than those of resistance-shift and shape-change switches. Remarkably, this rapid t_1 exceeds that of gas/smoke sensors by 151 times. The exceptionally fast response time underscores the sensitivity and efficiency of our TMLM thermal switch.

The temperature and shape variation of the TMLM-20% droplet as it falls at $T_H = 85$°C were further analyzed by finite element simulation (detailed in Supplementary Figs. 13–16, Table 2, and Movie 5). Upon heat exposure for 200 ms, the temperature of TMLM droplet within the tube experiences an initial increase (Fig. 4e and Supplementary Fig. 15). Notably, the temperature of TMLM droplet surpasses that of the thermal fluid, attributed to the high thermal conductivity of LM (25.4 W m^{-1} K^{-1})[14]. Subsequently, the T_{LM} quickly reaches ~60°C after 520 ms, becoming ellipsoidal. It then starts detaching from the top at 540 ms, completing its descent to the bottom at 620 ms. Moreover, a further analysis of the magnetic flux density (**B**) within the droplet and drop speed (v) of TMLM-20% (Supplementary Fig. 16) as depicted in Fig. 4f presents the stability of the parameters T_{LM}, **B**, and v within the initial 110 ms. This stability is attributed to the transfer of external heat to the interior through the glass tube and thermal fluid. Then, the T_{LM} gradually increases while **B** decreases, which is attributed to the thermal-induced magnetic transition. A minor T_{LM} peak emerges around 62°C at 520 ms, signifying the critical response temperature of the TMLM droplet. At the same time, v shows a sharp peak of 4.5 cm s^{-1}, corresponding to the falling of TMLM droplet. The v then diminishes to 0 at 620 ms, indicating the completion of the falling process. This modeled drop time of 620 ms is in good agreement with the experimental value (660 ms, $T_H = 85$°C), thereby affirming the reliability of the experimental response time. Consequently, the above results prove that our designed miniature micro-channel TMLM thermal switch can achieve two functions of thermal-triggered connection or disconnection with a fast response time.

A fast bidirectional TMLM thermal switch technology for practical applications

The aforementioned micro-channel thermal switch serves as the basis for our further design, which involves connecting two electrical circuits at the upper and lower ends. This modification allows for the bidirectional response of the TMLM thermal switch to be realized (see Fig. 5a). The experiment depicted in Supplementary Movie 4 demonstrates that the TMLM droplet initially moves to the upper end due to magnetic attraction, thereby completing the upper circuit and activating LED 1. Meanwhile, LED 2 at the lower end remains OFF due to the lack of connectivity. Upon reaching the temperature above the T_C of the TMLM, the droplet descends to the bottom, causing LED 1 to turn OFF and LED 2 to illuminate (ON). Figure 5b shows the corresponding experimental results of the system. At RT, the blue LED in the upper circuit is illuminated (ON) while the red LED in the lower circuit remains unlit (OFF). Upon the addition of hot water to the beaker, the thermal switch is heated, causing the TMLM droplet to detach. This results in the deactivation of the blue LED (OFF) and the activation of the red LED (ON). Notably, finite element simulation results indicate that the transition from the disconnection of the upper circuit to the conduction of the lower circuit occurs in a mere ~100 ms. This brief timespan underscores the thermal switch's ability to achieve instantaneous bidirectional response.

Figure 5c, d presents a comparative analysis of the response process of a commercial thermal switch, referenced as KSD9700C,
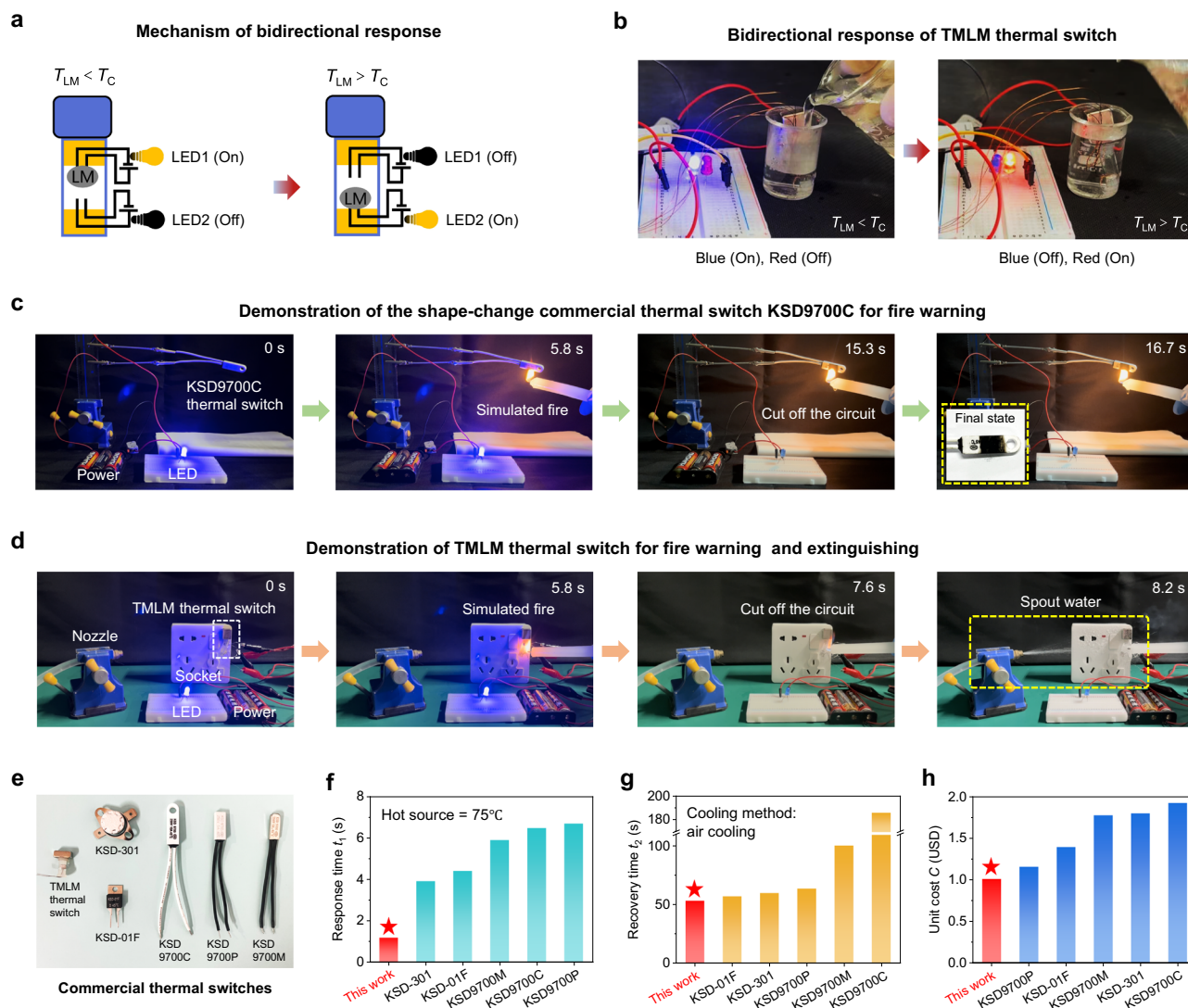
Fig. 5 | Fast bidirectional response and practical applications of TMLM thermal switch, as well as the comprehensive comparison with typical commercial thermal switches. a Schematic illustration of the working principle of the bidirectional response of TMLM thermal switch. **b** Experimental demonstration of bidirectional response of TMLM thermal switch. **c** Demonstration of the shape-change commercial thermal switch KSD9700C for fire warning. **d** The practical application demonstration of TMLM thermal switch for fire warning and extinguishing. **e** Images of TMLM thermal switch and typical commercial thermal switches. **f**–**h** Comparison of (**f**) response time t_1, (**g**) recovery time t_2, and (**h**) unit cost C of TMLM thermal switch with those of typical commercial thermal switches. (Source data are provided as a Source Data file).

versus our designed TMLM thermal switch in the context of a fire event. The process is visually detailed in Supplementary Movies 6 and 7. The KSD9700C switch primarily functions by utilizing the deformation of its internal spring sheet during heating to interrupt the circuit. This commercial thermal switch design is widely used in our daily life and industrial applications. As shown in Fig. 5c, the LED electrical circuit remained operational (ON) initially. At 5.8 s, a candle was introducd beneath the KSD9700C switch to emulate circuit overheating. Subsequently, the KSD9700C switch reacted at 15.3 s, disconnecting the LED electrical circuit. This observation indicates a 9.5 s response time for the commercial thermal switch to deactivate the electrical circuit following the onset of the fire. Moreover, its unidirectional response functionality restricts its capability to solely disable the LED electrical circuit without the capacity to independently initiate fire extinguishing actions. On the contrary, as shown in Fig. 5d and Supplementary Movie 7, upon introducing the candle under the TMLM thermal switch at 5.8 s, it promptly responded at 7.6 s to terminate the electrical circuit while simultaneously activating the fire shower, extinguishing the fire at 8.2 s. Compared to the KSD9700C

switch with a response time of 9.5 s, the TMLM thermal switch achieves circuit deactivation 5.3 times faster, requiring a mere 1.8 s since the onset of the fire. Furthermore, it accomplishes fire suppression in only 2.4 s. Although the response time of a thermal switch may vary depending on the nature and environment of the fire, the above results obtained under the same conditions demonstrate that this TMLM thermal switch shows a significantly faster response time than conventional thermal switches. Thus, it allows for faster activation of alarms and protective measures (such as triggering fire suppression systems), significantly reducing the risk of damage or injury in critical situations. This outcome underscores the remarkably improved response capabilities of the TMLM thermal switch in swiftly terminating the circuit and triggering the fire suppression measures, indicating its potential to enhance fire safety systems. In addition to the fast bidirectional response, the TMLM droplet can convert back to FM state during cooling and return to its original state, thus realizing multiple recycling.

An evaluation of our TMLM thermal switch, compared with five typical commercial thermal switches (see Supplementary Table 3) with

operating temperatures (45 °C) close to the T_C of our TMLMs (43 °C), indicates that the TMLM thermal switch is compact and suitable for use in confined space or micro-circuits as shown in Fig. 5e. Additionally, a comprehensive comparison of the response time (t_1), recovery time (t_2), and unit cost (C) between the TMLM thermal switch and typical commercial thermal switches (Fig. 5f) demonstrates that our TMLM thermal switch exhibits the shortest response time t_1 of 1.2 s under the same T_H of 75 °C. Although the t_1 of 1.2 s may be slower than some millisecond-level devices, it is still 3.3 – 5.6 times faster than typical commercial thermal switches. As the T_H increases, the t_1 of our TMLM thermal switch can also reach milliseconds (Fig. 4d), thus showing a fast response characteristic. In applications such as fire safety or overheating protection systems, a faster response time means quicker disconnection of the electrical circuit or activation of fire suppression systems in the first few seconds after ignition. This significantly reduces the risk of property damage, injury, or even loss of life, effectively meeting the urgent need for fast responsed thermal switches. Moreover, in Fig. 5g, it is evident that the TMLM thermal switch demonstrates the fastest recovery time t_2 of 53.6 s among all thermal switches considered. Notably, this t_2 value is 3.5 times faster than that of KSD9700C switch. Moreover, we have demonstrated that this t_2 can be further reduced to 21 s or 4 s by using cold air or ice water cooling instead of air cooling (see Supplementary Movie 2). This fact highlights the substantial impact of the cooling environment on the recovery time. In addition, owing to the minimal amount of liquid metal and low raw material cost, the unit cost (C) of the TMLM thermal switch, as shown in Fig. 5h, is the lowest at ~1.016 USD (detailed cost calculations are shown in the Supplementary Notes). This cost reflects raw material expenses in a laboratory setting and does not include processing or molding costs, and we expect that the cost of this TMLM thermal switch can be further reduced with large-scale manufacturing. So it would be more cost-effective than other thermal switches after commercialization. These benefits underscore the enormous potential of our TMLM thermal switch in the field of thermal management. Furthermore, we built a cycle life test device and carried out a cyclic test to verify the cyclic stability of the TMLM thermal switch (Supplementary Fig. 17). After 200 heating and cooling cycles, the TMLM thermal switch still retains good temperature sensitivity and fast response capability, demonstrating excellent durability and stable performance over extended use.

It is worth noting that this ferromagnetic transition TMLM can also find application in many other various fields, such as direct 3D printing on various substrates and function as flexible thermal switches (Supplementary Figs. 18–21, Movies 8 and 9); fast response temperature sensors and full supervision of refrigerated transportation in industry (Supplementary Fig. 22); magnetic refrigeration technology based on the magnetocaloric effect, and efficient heat dissipation of micro-size devices (Supplementary Fig. 23). Therefore, the diverse capabilities of this ferromagnetic transition TMLM will have a broader range of potential application beyond thermal switches in future.

Discussion
Thermal switches are important for detecting malfunctions in a broad variety of devices. They are instrumental in preventing significant economic damage and saving lives in the case of equipment overheating. The key parameters for optimal performance include response time and operation temperature. In addition, reactivation after the issue is resolved and the ability to independently activate countermeasures are significant enhancements for thermal switches. In this work, we designed a TMLM thermal switch with a fast bidirectional response by creating a thermomagnetic liquid metal. This material has good fluidity, appropriate viscosity, and high electrical conductivity. It can be tuned to actuate at different temperatures, and the proposed design enables simultaneous detection of thermal

malfunctions and activation of countermeasures. It shows a fast response time t_1 of 1.2 s under the same T_H of 75 °C, which is 3.3 – 5.6 times faster than typical commercial thermal switches. Moreover, it can be further reduced to 660 ms under the optimal environment. Besides, the TMLM thermal switch also has the fastest recovery time t_2 of 53.6 s compared with the commercial thermal switches, and this t_2 can be further reduced to 4 s using ice water cooling. Meanwhile, it still retains good temperature sensitivity and fast response capability after 200 heating and cooling cycles. Despite its enhanced performance and added functionality, this thermal switch incorporating the TMLM is estimated to cost only ~1.02 USD for each. The intrinsic properties of the TMLM also make it suitable for applications beyond this thermal switch in the future.

Methods
Raw materials
The raw materials of Ni, Mn, and In with purity higher than 99.5 wt.% were purchased from Beijing Jiaming Platinum Nonferrous Metals Co., Ltd. The commercial Galinstan ($Ga_{68.5}In_{21.5}Sn_{10}$) liquid metals (LMs) with a theoretical melting point of ~11 °C were purchased from Dongguan Houjie Dingtai Metal Materials Co., Ltd. The thermal fluid was purchased from Sichuan Wuxiandian Technology Co., Ltd. This thermal fluid is a commercial diamond nanofluid with a thermal conductivity of 1.0917 W m^{-1} K^{-1}, and it is also non-conductive and non-corrosive and usually be used as a coolant. Customized quartz glass tubes of different specifications were purchased from Donghai County Shengyi Quartz Products Co., Ltd. Rubber stoppers of different specifications were purchased from Kunshan Wanjianguangmang Hardware and Electrical Co., Ltd. Customized N52 magnets were purchased from Ganzhou Ruitong Magnetic Materials Co., Ltd.

Preparation and characterization of Ni-Mn-In particles
$Ni_2Mn_{1.4}In_{0.6}$ (Ni-Mn-In) and $Ni_{1.58}Mn_2In_{0.42}$ alloys were prepared by induction-melting the pure components with a purity higher than 99.5 wt.% under an argon atmosphere. The as-cast ingots were both sealed in a high-vacuum quartz tube and annealed at 900 °C for 7 days ($Ni_2Mn_{1.4}In_{0.6}$) and 800 °C for 2 days ($Ni_{1.58}Mn_2In_{0.42}$), followed by quenching in ice water. The ingots were then crushed into large particles with an iron pestle, manually pounded into powders using a mortar, and sieved through a 300-mesh screen.

The size distribution was measured by dynamic light scattering with Malvern Mastersizer 2000 laser particle size analyzer. The microstructure was studied by a Merlin VP Compact field emission scanning electron microscope (SEM), and the elemental analysis was investigated by energy-dispersive spectroscopy (EDS). Phase analysis was performed and lattice parameters were determined by room-temperature X-ray powder diffraction (XRD) using Ultima IV diffractometer with Cu $K_{\alpha 1}$ radiation, the scan rate was 10° min^{-1}.

Synthesis of thermo-magnetic liquid metals (TMLMs)
The magnetic modification process for obtaining the TMLMs is illustrated in Fig. 2a, which can be specified as the following steps. First, we added about 10 g Galinstan liquid metal into a clean beaker by using a pipette gun. Next, the suitable mass of Ni-Mn-In particles were added to Galinstan LM, and then the beaker was shaken until the surface of Galinstan was coated with a uniform layer of Ni-Mn-In particles. Then, TMLMs were made by vigorously stirring galinstan and Ni-Mn-In particles. It takes about 15 – 30 min to fully internalize the particles, depending on the packing fraction of Ni-Mn-In particles. Finally, TMLMs were sonicated for 2 min to make the Ni-Mn-In particles evenly distributed in the LM and improve the stability of the TMLMs. It should be noted that we prepared the TMLMs by directly mixing LM and Ni-Mn-In particles in air rather than in HCl or NaOH solutions as reported in most works[28,41], in order to prevent LM and Ni-Mn-In particles from reacting in these solutions.

Microstructure characterization of TMLMs

Differential scanning calorimetry (DSC) measurements were carried out using a DSC 6220 with a heating/cooling rate of 10 K min⁻¹, and DSC/TG Pan Al_2O_3 crucibles were used as sample holders. X-ray diffraction (XRD) was conducted using a Bruker D8 Advance X-ray diffractometer with a scan rate of 2° min⁻¹. The microstructure was studied by a ZEISS GeminiSEM 300 Compact field emission scanning electron microscope (SEM), and the elemental analysis was performed by energy-dispersive spectroscopy (EDS). The room temperature high-resolution transmission electron microscopy (HRTEM) images, selected area electron diffraction (SAED) patterns, and the in-situ TEM images at room temperature were obtained by a JEM F200 transmission electron microscope (TEM) from Japan Electronics Co., Ltd (JEOL). The TMLM-20% was dropped onto a molybdenum mesh for TEM measurement. The contact angles were measured by contact angle meter (TBU 90E). The micro-CT analysis was performed by three-dimensional X-ray microscopy (GE Vtomex). The TMLM-20% was sealed and filled in a cylindrical plastic container with a size of Φ 2 × 3.5 mm. Tomographic images of TMLM-20% cross-section without image overlap were obtained, which were exported every 2.4 μm. Finally, 3D images can be constructed by stacking multiple tomographic images. The scanning voltage is 120 kV, the current is 120 μA, and the resolution is 2.4 μm. The density of sample, measured by the Archimedes method, was 7.935 g cm⁻³ for Ni-Mn-In alloy.

Magnetic and electric measurement of TMLMs

The magnetization was measured using a cryogen-free cryocooler-based physical property measurement system (model VersaLab) from Quantum Design Inc. The magnetization isotherms were measured by adopting a loop process with the magnetic field change of up to 3 T. The magnetization and demagnetization rate were 0.01 T s⁻¹. The electrical conductivities were tested using a Puchun DDS-11C electrical conductivity meter with automatic temperature replenishment at room temperature of 20 °C.

Rheological measurement of TMLMs

The rheological properties of TMLMs were characterized by using a Haake Mars40 rotational rheometer with a diameter of 20 mm parallel-plate geometry. The viscoelasticity test was conducted in amplitude sweep mode and the angular frequency was a constant 10 rad s⁻¹. The apparent viscosity test was conducted in steady-state mode and the variation of shear stress from the sample was monitored when applying an increasing shear rate from 0.1 to 1000 s⁻¹. In the two systems, the gap distance between two plates was both fixed to 1 mm and the temperature was maintained at 25.00 ± 0.01 °C during measurements. The sample was transferred to the bottom plate with a diameter of 1 cm to avoid the preshear before the test. Each test was carried out 3 times to eliminate the random error.

Fabrication of micro-channel TMLM thermal switch

Firstly, a small TMLM-20% droplet of ~30 μL was placed inside a thin glass tube with the size of Φ 5 × 20 mm (thickness is 0.5 mm). The glass tube was filled with a commercial thermal fluid to improve heat transfer, and the detailed parameters of commercial thermal fluid have been shown in "Materials" section. It should be pointed out that the droplet can be lifted up by a magnetic field $\mu_0 H$ lower than 200 mT, which is favorable for practical application. Meanwhile, the length of plug is adjusted to be 3.5 mm by analyzing the variation of magnetic flux density **B** as a function of distance between magnet and droplet (Supplementary Fig. 10). A small magnet with maximum field of 0.4 T was fixed to the upper surface of the rubber stopper with high-temperature glue. At the initial state with the temperature of TMLM-20% droplet lower than its T_C, the droplet was attracted to the top end of the tube by the magnet, thus connecting the circuit of LED. When the temperature rises beyond T_C, the droplet will fall to the bottom due

to the thermal-induced magnetic transition of TMLM-20%, and so it leads to the disconnection of LED circuit. Similarly, it can be also designed as a thermal-triggered conduction switch by locating the LED circuit at the bottom end. In this case, the LED will be turned on rather than turned off when the droplet falls off due to overheating. Finally, the bidirectional response of the TMLM thermal switch could be realized by connecting two electrical circuits on the upper and lower end.

Fabrication of the fire extinguishing simulation system

We placed the TMLM thermal switch in the upper right corner of a socket. The upper circuit of the TMLM thermal switch was connected to a LED, and the lower circuit was connected to the self-priming pump. The water pipe at the water inlet of the self-priming pump was placed in a cold water bucket, and the water outlet of the self-priming pump was connected to the nozzle through the water pipe. We used a candle as a simulated fire source to trigger the TMLM thermal switch.

Finite element analysis of the falling of TMLM-20% droplet

The falling of TMLM-20% droplet during heating was investigated using finite element simulations by the COMSOL Multiphysics software (Version 6.1). The laminar flow (spf) module, level sets (ls) module, magnetic field (mf) module in AC/DC, heat transfer of solid and fluid (ht) module, and multiphysics module were selected. The simulation process was carried out by the following steps:

Step 1: Build the two-axis symmetry model of the TMLM thermal switch with the size parameters as input (Supplementary Table 2).

Step 2: Specify the material properties of each part and input the parameters (Supplementary Table 2). The parameters of air, N52 magnet, and rubber stopper are derived from the built-in material parameters. TMLM-20% and thermal fluid are independently defined by adding empty materials.

Step 3: Employ the heat transfer module of COMSOL to simulate the variation of TMLM-20% temperature during heating, i.e., $T-t$ curves.

Step 4: Employ the magnetic field module to calculate the value of magnetic flux density **B** as a function of time based on the above simulated $T-t$ curves and the experimental $M-T$ curves (Fig. 3e).

Step 5: Employ the laminar flow module and level set module to simulate the variation in contact angle and surface tension of TMLM-20%.

Step 6: Wetted wall (ww), two phase flow coupling (tpf) and magnetohydrodynamics (mhd) models were added to the multiphysics model.

Step 7: The COMSOL conducts the study on phase initialization, then simulates the falling of TMLM-20% based on the change of magnetic flux density **B**, contact angle, and surface tension during heating.

Data availability

The data generated in this study are provided in the Source Data file. Source data are provided with this paper.

References

1. Li, X., Vázquez-López, A., Sánchez del Río Sáez, J. & Wang, D.-Y. Recent advances on early-stage fire-warning systems: Mechanism, performance, and perspective. *Nano-Micro Lett.* **14**, 106–136 (2022).
2. Wu, Q. et al. Efficient flame detection and early warning sensors on combustible materials using hierarchical graphene oxide/silicone coatings. *ACS Nano* **12**, 416–424 (2017).
3. He, S. et al. Prediction and early warning method of electrical fire risk based on firefighting big data. *J. Tsinghua Univ. (Sci. Technol.)* **64**, 478–491 (2023).
4. Ding, Z. et al. Thermoelectrics and thermocells for fire warning applications. *Sci. Bull.* **68**, 3261–3277 (2023).

5. Fonollosa, J., Solórzano, A. & Marco, S. Chemical sensor systems and associated algorithms for fire detection: A review. *Sensors* **18**, 553 (2018).

6. Evans, D. D. & Stroup, D. W. Methods to calculate the response time of heat and smoke detectors installed below large unobstructed ceilings. *Fire Technol.* **22**, 54–65 (1985).

7. Ma, Z. et al. A highly fire-retardant rigid polyurethane foam capable of fire-warning. *Compos. Commun.* **29**, 101046 (2022).

8. Zhang, L., Huang, Y., Dong, H., Xu, R. & Jiang, S. Flame-retardant shape memory polyurethane/MXene paper and the application for early fire alarm sensor. *Compos. Part B* **223**, 109149 (2021).

9. Jia, J., Wang, J. & Wang, Y. Shape memory polymer-based thermal-responsive circuit switches. *J. Mater. Chem. C.* **11**, 6276–6289 (2023).

10. Chen, J. et al. An ultrasensitive fire-warning chitosan/montmorillonite/carbon nanotube composite aerogel with high fire-resistance. *Chem. Eng. J.* **399**, 125729 (2020).

11. Deng, X. et al. Self-healable and recyclable dual-shape memory liquid metal-elastomer composites. *Polymers* **14**, 2259 (2022).

12. Kondoh, Y. et al. High-reliability, high-performance RF micromachined switch using liquid metal. *J. Microelectromech. Syst.* **14**, 214–220 (2005).

13. Duan, L. et al. Surface optics and color effects of liquid metal materials. *Adv. Mater.* **35**, 2210515 (2023).

14. Wang, D. et al. Liquid metal combinatorics toward materials discovery. *Adv. Mater.* **35**, 2303533 (2023).

15. Wang, Q. et al. Magnetoactive liquid-solid phase transitional matter. *Matter* **6**, 1–18 (2023).

16. Idrus-Saidi, S. A. et al. Liquid metal synthesis solvents for metallic crystals. *Science* **378**, 1118–1124 (2022).

17. Wang, S. et al. Intrinsically stretchable electronics with ultrahigh deformability to monitor dynamically moving organs. *Sci. Adv.* **8**, eabl5511 (2022).

18. Zhao, Y. et al. A self-healing electrically conductive organogel composite. *Nat. Electron.* **6**, 206–215 (2023).

19. Lu, Y. et al. Mussel-inspired multifunctional integrated liquid metal-based magnetic suspensions with rheological, magnetic, electrical, and thermal reinforcement. *ACS Appl. Mater. Interfaces* **13**, 5256–5265 (2021).

20. Li, X. et al. Programmable digital liquid metal droplets in reconfigurable magnetic fields. *ACS Appl. Mater. Interfaces* **12**, 37670–37679 (2020).

21. Hu, L. et al. Magnetic liquid metals manipulated in the three-dimensional free space. *ACS Appl. Mater. Interfaces* **11**, 8685–8692 (2019).

22. Shen, Y. et al. Reactive wetting enabled anchoring of non-wettable iron oxide in liquid metal for miniature soft robot. *Nat. Commun.* **14**, 6276 (2023).

23. Lu, Y. et al. Magnetically tightened form-stable phase change materials with modular assembly and geometric conformality features. *Nat. Commun.* **13**, 1397 (2022).

24. Jeon, J., Lee, J.-B., Chung, S. K. & Kim, D. On-demand magnetic manipulation of liquid metal in microfluidic channels for electrical switching applications. *Lab Chip* **17**, 128–133 (2017).

25. Lyange, M. V., Barmina, E. S. & Khovaylo, V. V. Structural and magnetic properties of Ni-Mn-Al Heusler alloys: a review. *Mater. Sci. Found.* **81-82**, 232–242 (2015).

26. Hu, F., Shen, B., Sun, J. & Wu, G. Large magnetic entropy change in a Heusler alloy$Ni_{52.6}Mn_{23.1}Ga_{24.3}$single crystal. *Phys. Rev. B* **64**, 132412 (2001).

27. Singh, S. et al. Large magnetization and reversible magnetocaloric effect at the second-order magnetic transition in Heusler materials. *Adv. Mater.* **28**, 3321–3325 (2016).

28. Lu, Y. et al. Liquid metal-based magnetorheological fluid with a large magnetocaloric effect. *ACS Appl. Mater. Interfaces* **12**, 48748–48755 (2020).

29. Brechtl, J. et al. Compatibility of $LaFe_{13-x-y}Mn_xSi_yH_{1.6}$ and eutectic liquid GaInSn alloy. *Magnetochemistry* **10**, 13 (2024).

30. Castro, I. A. D. et al. A gallium-based magnetocaloric liquid metal ferrofluid. *Nano Lett.* **17**, 7831–7838 (2017).

31. Zhang, B. et al. Giant magnetothermal conductivity in the Ni–Mn–In ferromagnetic shape memory alloys. *Appl. Phys. Lett.* **91**, 012510 (2007).

32. Chen, H. et al. Excellent thermomagnetic power generation for harvesting waste heat via a second-order ferromagnetic transition. *Mater. Horiz.* **11**, 2603–2614 (2024).

33. Jin, M. et al. Internal friction of phase transformations observed around room temperature in Ga-In-Sn eutectic alloys. *Arch. Metall. Mater.* **60**, 2097–2100 (2015).

34. Zhang, C. et al. Study on the nucleating agents for gallium to reduce its supercooling. *Int. J. Heat. Mass Transf.* **148**, 119055 (2020).

35. Egry, I., Ricci, E., Novakovic, R. & Ozawa, S. Surface tension of liquid metals and alloys — Recent developments. *Adv. Colloid Interface Sci.* **159**, 198–212 (2010).

36. Cui, C. et al. Reconfigurable 4D printing of reprocessable and mechanically strong polythiourethane covalent adaptable networks. *Adv. Funct. Mater.* **32**, 2203720 (2022).

37. Liu, W., Chen, H., Ge, M., Ni, Q.-Q. & Gao, Q. Electroactive shape memory composites with TiO_2 whiskers for switching an electrical circuit. *Mater. Des.* **143**, 196–203 (2018).

38. Luo, H. et al. Temperature sensing of conductive shape memory polymer composites. *Mater. Lett.* **140**, 71–74 (2015).

39. Chen, L. et al. 3D printable robust shape memory PET copolyesters with fire safety via π-stacking and synergistic crosslinking. *J. Mater. Chem. A* **7**, 17037–17045 (2019).

40. Xie, H. et al. A highly efficient flame retardant nacre-inspired nanocoating with ultrasensitive fire-warning and self-healing capabilities. *Chem. Eng. J.* **369**, 8–17 (2019).

41. Tang, J., Zhao, X., Li, J., Zhou, Y. & Liu, J. Liquid metal phagocytosis: Intermetallic wetting induced particle internalization. *Adv. Sci.* **4**, 1700024 (2017).

Acknowledgements

Author contributions

Conceptualization: K.M.Q., F.X.H., B.G.S., K.C., V.F., J.Y.L.[1], H.Z. Methodology: H.D.C., Y.Y.X., Z.Y.Y., J.Y.L[2]. Investigation: H.D.C., Y.Y.X., K.M.Q., L.L.X., Z.Y.Y., C.Y.X., H.Z. Visualization: H.D.C., K.M.Q., M.Z.L., H.Z. Funding acquisition: H.Z., K.M.Q., K.C., J.L., V.F., B.G.S., F.X.H. Project administration: H.Z. Supervision: H.Z., B.G.S. Writing – original draft: H.D.C. Writing – review & editing: H.Z., J.Y.L.[1], V.F., J.L., Y.Y.L. All authors discussed the experiments, read and commented on the manuscript. (J.Y.L.[1] stands for Jia Yan Law, and J.Y.L.[2] stands for Jingyi Liu)

Competing interests

The authors declare no competing interests.

Additional information

Supplementary information The online version contains supplementary material available at https://doi.org/10.1038/s41467-025-58015-x.

Correspondence and requests for materials should be addressed to Hu Zhang.

Peer review information *Nature Communications* thanks Daeyoung Kim, and the other, anonymous, reviewers for their contribution to the peer review of this work. A peer review file is available.

Reprints and permissions information is available at http://www.nature.com/reprints

Publisher's note Springer Nature remains neutral with regard to jurisdictional claims in published maps and institutional affiliations.